



NRL/MR/6040--17-9760

# **Equilibrium Wall-Model Implementation in a Nodal Finite Element Flow Solver JENRE for Large-Eddy Simulations**

JUNHUI LIU

ANDREW T. CORRIGAN

KAZHIKATHRA KAILASANATH

*Laboratory for Propulsion, Energetic, and Dynamic Systems*

*Laboratories for Computational Physics and Fluid Dynamics*

November 13, 2017

Approved for public release; distribution is unlimited.





## Table of Contents

I.	Introduction.....	1
II.	Large-Eddy Simulation Methodology and Equilibrium Wall Model .....	1
III.	A Boundary-Layer Flow At $M_\infty = 0.9$ on a Flat Plate .....	2
A.	Using cubic cells .....	3
1.	Comparison with the measurement data.....	3
2.	Shape factor calculation .....	3
3.	Benefits of using a non-zero surface tangential velocity .....	4
B.	Using cells of large aspect ratios .....	4
IV.	Boundary-Layer Flows in a C-D Nozzle .....	4
V.	Conclusions.....	5
VI.	Acknowledgements .....	6



## **Executive Summary**

The equilibrium wall model is implemented in a nodal finite element flow solver JENRE developed at the Naval Research Laboratory. The Crocco-Busemann relation is used to account for the compressibility. In this wall-model implementation, the first cell adjacent to the wall is used to estimate the shear stress on the wall. The no-slip adiabatic boundary condition is applied to the inviscid and viscous fluxes on the wall to satisfy the surface physical condition, but a non-zero surface tangential velocity is used in the calculation of the volume and surface integrals in a cell adjacent to the wall. This is because using a zero-surface velocity will grossly underestimate these integrals due to the linear basis function used in JENRE. This implementation is validated in a subsonic boundary-layer flow over a flat plate and a supersonic flow in a converging and diverging nozzle used frequently in our jet noise simulations. Skin frictions, velocity profiles and turbulence quantities predicted by the current wall-model implementation agree well with available experimental data and theoretical models. The grid convergence is excellent. Grid sizes much larger than those recommended in other wall-model implementations can be used. The current wall-model implementation has not encountered the numerical problem associated with using the first cell as reported in other wall-model implementations. The volume and surface integrals based on the non-zero surface velocity in a cell adjacent to the wall show a good agreement with those derived from the equilibrium boundary-layer velocity profile and the density profile based on the Crocco-Busemann relation.



# Equilibrium Wall-Model Implementation in a Nodal Finite Element Flow Solver JENRE for Large-Eddy Simulations

## I. Introduction

Using large-eddy simulations (LES) to resolve wall-bounded flows at high Reynolds numbers is computationally prohibitive due to the limitations of the numerical methods and computational resources. The major bottleneck is to resolve the inner layer in the boundary layer near the wall. It is a region where most of the turbulence production takes place and turbulent eddies are created. According to Piomelli and Balaras [1], 99% of the grid points are used to resolve an inner layer which thickness is only 10% of the boundary layer at a Reynolds number of  $10^6$ . The number of the grid points required in the outer layer increases with the Reynolds number as  $Re^{0.5}$ , but the number of the grid points in the inner layer increases as  $Re^{2.4}$  [2]. In addition, this very fine grid resolution imposes a severe constraint on the time-step size. To make LES applicable to wall-bounded flows at high Reynolds numbers, attempt to bypass the inner layer and model its effects in a global sense have been used since the pioneering work by Deardorff [1] and Schumann [4]. Three classes of modeling the inner layer have been proposed and developed [1]-[5]. The least expensive method is the equilibrium wall-model approach, which assumes the existence of an equilibrium layer in which the shear stress is constant. This assumption results in the existence of a logarithmic layer that can be used to compute the wall stress from the velocity in the outer layer. Other two classes are the zonal method and the hybrid method. Both of them require the computation of separate, but simplified, flow equations in the inner layer. More information regarding the wall-modeling effort can be found in reviews by Piomelli and Balaras [1], Piomelli [2] and Spalart [5]. Since the wall-model method models the effect of the inner layer on the outer layer, it is possible to introduce some numerical errors. It has been reported that the wall-model method often encounters “log-layer mismatch” and 10%-15% error in skin-friction prediction. These types of numerical discrepancies can be observed in all three wall-model implementations. In the equilibrium wall-model approach, large numerical discrepancies are often observed when the first grid point above the wall is used to estimate the wall shear stress. It has been recommended to use grid points further above the wall to improve the prediction [6].

Our in-house LES Solver JENRE (**J**et **E**ngine **N**oise **R**eduction) uses a nodal finite-element method built upon unstructured meshes. Since implementing the zonal and hybrid methods requires significant changes to the solver, the equilibrium wall-model method is used in the current wall-model implementation. It should be mentioned that the reported numerical issues associated with the wall-model method come from simulations using either finite-difference or finite-volume solvers. The implementation in finite-element flow solvers for large-eddy simulations has rarely been reported. In this work, we first examine the performance of the equilibrium wall-model method in a subsonic boundary-layer flow over a flat plate at  $M_\infty = 0.9$ . The results are compared with available experimental data. Since JENRE has been used frequently in supersonic jet noise simulations [7]-[10], this wall-model method is also tested in a supersonic flow inside a converging and diverging (C-D) nozzle.

## II. Large-Eddy Simulation Methodology and Equilibrium Wall Model

The compressible Navier-Stokes equations can be written as

$$\frac{\partial Q}{\partial t} + \nabla \cdot (F^a(Q) - F^v(Q)) = 0, \quad (1)$$

where  $Q$  is the vector of the conservative variables,  $F^a$  is the inviscid flux vector and  $F^v$  is the viscous flux vector. The definitions of those terms can be found in any text books of computational fluid dynamics. Eq. (1) is solved by the Taylor-Galerkin nodal finite element method implemented in JENRE. Taylor-Galerkin finite element method maintains the second order spatial accuracy even on irregular, unstructured tetrahedral meshes, which is often difficult to achieve using finite volume methods. In addition, the nodal method requires less computational memory than the cell-centered method because it requires a smaller number of degrees of freedom in tetrahedral meshes. In the current version of JENRE, the linear basis function is used for the spatial discretization, and the finite element flux corrected transport (FEM-FCT) method is used for the flux integration and limiting calculations [11][12]. The multi-dimensional FEM-FCT flux limiter provides an implicit subgrid stress model, and the methodology is in the



category of the Monotonically Integrated Large-Eddy Simulation (MILES) approach. The tetrahedral mesh is used because of its simplicity and the accurate representation of complex geometries.

The velocity profile in an equilibrium boundary layer has two distinct layers as shown in Figure 1. The velocity near the wall can be modeled as a linear function of the distance to the wall, but slightly away from the wall, the velocity distribution follows a logarithmic function. The equilibrium wall-model method uses the information in the logarithmic layer to model the effect of the inner layer on the out layer. In this approach, the viscous shear stresses on the wall surface are not computed from velocity gradients near the wall. They are estimated from the logarithmic velocity profile [13]:

$$u^+ = \frac{U}{u_\tau} = \frac{1}{\kappa} \ln(y^+) + B, \quad (2)$$

where  $\kappa = 0.41$  and  $B = 5$ .  $u_\tau$  is the friction velocity and  $u_\tau = \sqrt{\tau_w/\rho_w}$ . The parameters  $\tau_w$  and  $\rho_w$  are the shear stress and density on the wall. In addition,  $u^+$  and  $y^+$  are the velocity and distance expressed in wall units, where  $u = U/u_\tau$  and  $y^+ = \rho_w u_\tau y/\mu_w$ . The parameter  $\mu_w$  is the viscosity at the wall. The wall shear stress  $\tau_w$  is computed from Eq. (2) based on the tangential velocity  $U$  of a given grid point located in the logarithmic layer. Because the velocity and the heat flux on the wall are zero on an adiabatic wall surface, the contribution of surface fluxes to the flow is solely represented by the wall shear stress in this equilibrium wall-model method. Eq. (2) is derived from an incompressible velocity profile, and the density is assumed as a constant. The compressibility effect is thus taken into account by using the van Driest effective velocity formulation [13]. The velocity  $U$  in Eq. (2) is replaced by the van Driest effective velocity  $U_{eq}$ , which can be expressed as

$$U_{eq} = \sqrt{2C_p T_{aw}} \sin^{-1} \frac{U}{\sqrt{2C_p T_{aw}}} \quad (3)$$

at an adiabatic wall condition.  $T_{aw}$  is the adiabatic temperature on the wall, and  $C_p$  is the specific heat capacity. The first point above the wall would be a natural choice for the estimation of the wall shear stress. But as mentioned in the previous section that large numerical discrepancies associated with using the first point have been reported in many wall-model implementations. It has been suggested to use points located further above the surface, for example, the third or even the fifth point from the wall surface [6][15][16]. The implementation of this method is straightforward in solvers using structured meshes, but it could cause severe computation penalties in solvers using unstructured meshes coupled with parallel computing methods, for example JENRE. Thus, in the current wall-model implementation, the first cell near the wall surface is used to estimate the wall shear stress.

The no-slip adiabatic surface condition is applied to the inviscid and viscous fluxes on the wall to satisfy the surface physic condition. Since the current version of JENRE uses the linear basis function, using a zero-surface velocity would grossly underestimate the volume and surface integrals in a cell adjacent to the wall, for example, the integrals of mass, momentum and kinetic energy. To avoid this underestimation, a non-zero tangential surface velocity is used in those integrals. This tangential surface velocity is updated along with the flow field at interior nodes. It will be shown in the following section that the volume and surface integrals using a non-zero tangential surface velocity have a good agreement with integrals derived from the equilibrium boundary-layer velocity profile (shown in Figure 1) and the density profile based on the Crocco-Busemann relation. Of course, it would be a more ideal option to use the equilibrium boundary-layer velocity profile and the Crocco-Busemann relation for the velocity and density basis functions near the wall. However, this would require significant changes to the existing code. It could be considered in the future development.

### III. A Boundary-Layer Flow At $M_\infty = 0.9$ on a Flat Plate

Figure 2 shows the mesh distribution for this boundary-layer flow over a flat plate. Inflow turbulences are generated by surface roughness presented as surface bumps in the entrance region. The mesh inside the boundary layer is similar to a structured mesh except that each hexahedral cell is divided into several tetrahedral cells. This type of boundary-layer mesh makes it easier to generate cells with large aspect ratios, which may reduce the number of cells used in boundary layers when length scales of turbulence structures are significantly different in each direction. Another benefit of using this type of mesh is in the post processing, because the location of each node is predefined and no interpolation is needed in the data processing.

## A. Using cubic cells

Cubic cells where grid sizes are the same in all three directions are first tested. Table 1 shows mesh parameters of four grid resolutions at the axial location of  $Re_\theta = \rho_\infty U_\infty \theta / \mu_\infty = 31000$ , where  $\theta$  is the momentum thickness. Because the finest mesh requires a much larger number of grid points, the computational domain of the finest grid resolution extends only as far as  $Re_\theta = 22000$ . Thus, the mesh parameters of this grid resolution shown in Table 1 are estimated values. Figure 3 shows an instantaneous temperature distribution using the second coarsest mesh (mesh\_II) shown in Table 1. Disturbances are generated when the flow passes the surface roughness in the entrance region and the flow becomes turbulent some distance downstream. The axial length from the surface roughness area to the end of the plate is  $1.4\text{ m}$  in the three coarser simulations. The corresponding  $Re_\theta$  is roughly 44000.

### 1. Comparison with the measurement data

Figure 4 shows streamwise skin-friction evolution compared with an incompressible empirical relation [18] and incompressible measurement data [19]. To compare the present compressible flow results with incompressible skin frictions, the van Driest II transformation [6][13][14] is used to transform the compressible Reynolds number and skin friction into equivalent incompressible values,

$$C_{f,inc} = \frac{T_w/T_\infty - 1}{\arcsin^2 a} C_f, \quad a = \sqrt{1 - T_\infty/T_w}, \quad Re_{\theta,inc} = \frac{\mu_\infty}{\mu_w} Re_\theta, \quad (4)$$

where the skin friction  $C_f = 2\tau_w/(\rho_\infty U_\infty^2)$ . The four simulations present a very good grid convergence where the boundary layer is established. The magnitude and axial slope agree very well with those shown in measurement data. Figure 5 shows the comparison of streamwise velocity distributions. The distributions of the three coarser meshes are results at the location of  $Re_{\theta,inc} = 31000$ , where the boundary-layer thickness is roughly  $0.02\text{ m}$ . The result of the finest mesh is at the end of its computational domain at  $Re_\theta = 22000$ . Again, there is a very good grid convergence in the logarithmic layer, and the predictions show a good agreement with the measurement data and the logarithmic function. Figure 6 compares the turbulent intensities and the Reynolds shear stress. The numerical predictions agree reasonable well with the measurement data. As the grid resolution increases, more turbulence energy is captured and the peak location shifts further towards the wall. The differences shown near the boundary-layer edge are very likely introduced by the differences in the ambient turbulence levels. There are ambient turbulences in measurement data, but the ambient turbulences are not included in the numerical simulations.

### 2. Shape factor calculation

The shape factor is the ratio between the displacement thickness and the momentum thickness. It is an important factor to judge if the boundary-layer flow is laminar or turbulent. Laminar boundary layers have shape factors around 2.5, but turbulent boundary layers have lower shape factors between 1.3 and 1.8 [20]. Since the first cell size above the wall is not small in the wall-model approach, how to compute the mass and momentum integrals inside the first cell can significantly affect the shape factor. Two approaches are used in the shape-factor calculation. In the first approach, the velocity and density are approximated by linear functions of the normal distance in the first cell, but in the second approach, the velocity profile of the equilibrium boundary layer shown in Figure 1 and the Crocco-Busemann relation are assumed. Further above the wall, the velocity and density are approximated by linear functions inside each cell to be consistent with the methodology used in JENRE. Figure 7 presents the shape-factor distributions computed by these two approaches. If a linear approximation is used inside the first cell, the shape factors shown in Figure 7 (a) decrease in the axial direction, similar to the general trend observed in measurement data. The shape factors have large magnitudes, and they decrease as the grid resolution increases. The shape factors predicted by the two finer meshes are below 1.8 at some downstream locations. If judged by the results shown in Figure 7 (a), the boundary-layer flows predicted by the two coarser meshes are not yet turbulent. But if the velocity profile of the equilibrium boundary layer and the density profile based on the Crocco-Busemann relation are used in the first cell, the shape factor is much less sensitive to the grid resolution, as shown in Figure 7 (b). The axial variation is also small, and the shape factor is around 1.6 at all four grid resolutions. It would be interesting to see what the shape factor is if the mass and momentum integrations are computed based on the velocity profile of the equilibrium boundary layer and the Crocco-Busemann relation in the entire boundary layer. These integrations require the knowledge of the outer edge of the logarithmic layer. The distance at the outer edge of the logarithmic layer is between 5000 and 15000 wall units in the axial range shown in Figure 7, and the corresponding shape factor is between 1.59 and 1.56, respectively. These values are very close to the shape factors shown in Figure 7 (b). It should be mentioned that these integrations do not include the mass and momentum deficits beyond the logarithmic layer. However, because the contribution of the region beyond the logarithmic layer should be small in an

equilibrium turbulent boundary layer, it is not expected that the shape factor of an equilibrium turbulent boundary layer deviates significantly from the values shown above. It can be thus concluded that the boundary layers in these four simulations are turbulent in the axial range shown in Figure 7. This also brings up an issue associated with the shape-factor calculation. It is believed that the linear approximation between two neighboring vertical points has been used to compute the mass and momentum integrations in measurements. This may render caution in using measured shape-factor data. The physical locations of the measured points, especially the point adjacent to the wall, should be examined to see if they are appropriate for a linear approximation between two neighboring points.

### 3. Benefits of using a non-zero surface tangential velocity

As mentioned above, a non-zero tangential surface velocity is used in the volume and surface integrations in cells adjacent to the wall. Those integrations can be expressed as the mass integral  $\int \rho dy$ , the momentum integral  $\int \rho u dy$ , and the kinetic energy integral  $\int \rho u^2 dy$  in the first cell, where  $y$  is the direction normal to the wall. It is worthwhile to compare those integrals obtained from simulations based on a non-zero surface velocity and those derived from the velocity profile of an equilibrium turbulent boundary layer and the density profile derived from the Crocco-Busemann relation. Figure 8 and Figure 9 show comparisons of  $\int \rho u dy$  and  $\int \rho u^2 dy$  in the first cell. Predictions using the four grid resolutions are presented, and the results based on the linear shape function and the zero-surface velocity are also included. There is an excellent grid convergence and the axial variations are very small. The momentum integrals are only around 6% larger and the kinetic-energy integrals roughly 10% larger than those derived from the velocity profile of the equilibrium turbulent boundary layer and the density profile base on the Crocco-Busemann relation. This comparison should be considered very good since boundary-layer flows are not expected to follow those analytical functions exactly. The difference shown in the mass integrals  $\int \rho dy$  is even smaller (not shown), which is less than 1%. On the other hand, if the zero-surface velocity is used, the momentum and kinetic-energy integrals based on the linear basis function are grossly underestimated. These comparisons clearly demonstrate the effectiveness of using a non-zero surface velocity in the wall-model implementation in flow solvers using the linear basis function.

## B. Using cells of large aspect ratios

It is well known that turbulent structures near the wall are elongated in the streamwise direction in subsonic boundary layers over a flat-plate. Thus, the mesh type with a larger streamwise grid size is expected to be appropriate. This mesh type is tested and the streamwise grid size is fixed at a large value of  $\Delta x^+ = 370$ . The grid sizes ( $\Delta y = \Delta z$ ) in other two directions vary. Results of three aspect ratios ( $\Delta x^+ / \Delta y^+$ ), 1.0, 1.5 and 2.25, are shown in Figure 10. It can be seen that there is a good grid convergence and predictions agree well with both the measurement data and the logarithmic law. But if a very large spanwise mesh size is also used that  $\Delta z^+ = \Delta x^+ = 370$ , Figure 11 shows that the grid convergence is poor and the discrepancy increases as the normal size becomes smaller. This poor grid convergence probably is because this spanwise mesh size is too large for the elongated turbulence structures very near the wall in this subsonic boundary-layer flow. Grid sizes should be designed according to the turbulent structures.

## IV. Boundary-Layer Flows in a C-D Nozzle

JENRE has been used frequently to study supersonic jet noise at various jet operating conditions and nozzle geometries. For example, the noise generation in imperfectly expanded jets [8], the noise propagation in the presence of a deck and a jet blast deflector [9], and the assessment of noise reduction using chevrons [10]. The wall-model approach is thus tested in boundary layers inside the C-D nozzle used in those studies. It should be mentioned that there are non-zero pressure gradients inside the nozzle, so the flow is not truly equilibrium. But it may be argued that the non-equilibrium effect is accounted for by the velocity of the first node above the wall. The equilibrium wall-model method has been used previously by some researchers to simulate the boundary-layer effect in jet noise simulations, such as the work by Aikens, *et al.* [15] and Deniau, *et al.* [16]. Both studies use finite-difference solvers and both observed the numerical issue associated with using the first point above the wall. On the other hand, Guillaume *et al.* used a hybrid method to implement the boundary-layer effect in their jet noise simulations using a finite-volume solver [17]. As we have mentioned in the Introduction section, the wall-model implementation in a finite-element solver for large-eddy simulations has rarely been reported. To our best knowledge, this is the first time the application of a wall-model method to a finite-element solver being presented to the jet noise simulation community.

The nozzle geometry is shown in Figure 12, which is representative of practical supersonic military engine nozzles. The design Mach number  $M_d$  of this C-D nozzle is 1.5, and the fully expanded pressure ratio is 3.7. The nozzle pressure ratio ( $NPR$ ) is 4.0, which produces an underexpanded nozzle-exit condition. The Reynolds number based on the nozzle exit condition is slightly above four million. The boundary-layer thickness ( $\delta$ ) near the nozzle lip is roughly 1.2% of the nozzle-exit diameter ( $D$ ). Because the Reynolds number is high and the boundary layer is very thin, it is not practical to place many cells inside the boundary layer. Thus, tetrahedral meshes with large aspect ratios in both streamwise and spanwise directions are used to reduce the computational cost. The cell size in the principal flow direction is  $0.3\delta$  and  $0.33\delta$  in the circumstantial direction. They are indeed very large cell sizes, much larger than those reported in other wall-model implementations [6][15][16]. Three cell sizes in the normal direction are tested and they are shown in Table 2. The growth rate of the cell size is set to 1.05 in the two meshes where the normal grid size near the wall is smaller than the streamwise cell size. Because even the finest grid resolution only has 11~12 cells inside the boundary layer, all the three normal grid resolutions are coarse in terms of the boundary-layer simulation. Surface roughness is implemented in the subsonic region upstream of the C-D section to trip the boundary layer. The roughness height is 1% of the nozzle exit diameter, which is comparable to the boundary-layer thickness near the nozzle lip. Figure 13 shows the instantaneous vorticity contours inside and around the nozzle. Vortex structures are generated by the surface roughness, and they are stretched when they flow through the diverging section of the C-D nozzle due to the favorable pressure gradient. Figure 14 shows the velocity profiles at two axial locations upstream of the nozzle lip. There is a very good grid convergence when the wall model is applied. The velocity profiles align well with the logarithmic distribution given in Eq. (2). However, the unresolved boundary layers where the wall model is not implemented present much larger velocity deficits, which, as expected, decreases as the normal grid size decreases. It appears that the mesh type that has both large streamwise and spanwise aspect ratios performs well in this supersonic nozzle flow. This may indicate that turbulence structures in the outer layer given in these simulations have spanwise and streamwise lengths larger than the specified spanwise and streamwise cell sizes. Figure 15 shows turbulence intensity profiles of the axial velocity slightly downstream of the nozzle exit. Those results are interpolated from the data of unstructured grid nodes. It can be seen that the profiles predicted by the three grid resolutions are similar, except the peak location in the radial direction. The finer grid resolution predicts a peak radial location further from the jet center. This is consistent with the observation that the peak turbulence intensity shifts towards the wall as the grid resolution increases. It should also be mentioned that the current wall-model implementation observes a grid-to-grid oscillation in the axial direction in supersonic flows when the structured-like mesh is used. The oscillation magnitude increases as the grid aspect ratio increases, and a spatial averaging is needed to eliminate this numerical oscillation. But this numerical phenomenon is not present when an isotropic mesh is used. This probably is because the first node adjacent to the wall is not directly above the geometric center of the cell face on the wall in a structured-like mesh, but this is more likely so in an isotropic mesh.

## V. Conclusions

The equilibrium wall model is implemented in our in-house finite element flow solver JENRE to simulate the boundary-layer effect in flows at high Reynolds numbers. The Crocco-Busemann relation is used to account for the compressibility. The no-slip adiabatic boundary condition is applied to the inviscid and viscous fluxes on the wall to satisfy the surface physical condition. However, since the linear basis function is used in JENRE, a zero-surface-velocity would greatly underestimate the volume and surface integrals in the first cell adjacent to the wall comparing to those derived from the logarithmic velocity profile and the Crocco-Busemann relation. Thus, the surface tangential velocity is not forced to zero in those integrations. This surface tangential velocity is updated along with the flow field at interior points. This wall-model implementation is validated in a subsonic boundary-layer flow at  $M_\infty = 0.9$  over a flat plate and a supersonic flow in a C-D nozzle, which is used frequently in our previous jet noise simulations. The inflow turbulences are generated by surface roughness in both cases. It is found that this implementation presents an excellent grid convergence. It does not present the numerical issue associated with using the first-point as reported in other wall-model implementations. Grid sizes much larger than those recommended in other wall-model implementations can be used. Skin frictions, velocity profiles and turbulence quantities agree well with available experimental data and theoretical models. In addition, there is a very good agreement between the shape-factor predictions and those derived from the equilibrium turbulent boundary-layer velocity profile. Furthermore, there is a good agreement between the predicted volume and surface integrals in a cell adjacent to the

wall based on a non-zero tangential surface velocity and those derived from the equilibrium turbulent boundary-layer velocity profile and the density profile based on the Crocco-Busemann relation.

## VI. Acknowledgements

This research has been sponsored by the NRL 6.1 Computational Physics Task Area, as well as Office of Naval Research (ONR) through the Jet Noise Reduction (JNR) Project. Computing resources have been provided by the DoD High Performance Computing Modernization Program Office. The mesh is generated by using an open source mesh generator GMSH [21]. Authors are also thankful for the help provided by Prof. Kurt Aikens at the Houghton College in the wall-model validation.

## References

- [1]. Piomelli U, Balaras E. “Wall-layer models for large-eddy simulations. *Annu Rev Fluid Mech* 2002; 34:349–74.
- [2]. Piomelli U, “Wall-layer models for large-eddy simulations”, *Progress in Aerospace Sciences* 44 (2008) 437–446
- [3]. Deardorff J.W. “A numerical study of three-dimensional turbulent channel flow at large Reynolds numbers.” *J Fluid Mech* 1970; 41:453–80.
- [4]. Schumann U. “Subgrid-scale model for finite difference simulation of turbulent flows in plane channels and annuli.” *J Comput Phys* 1975; 18:376–404.
- [5]. Spalart, P.R., “Detached-eddy simulation,” *Annu. Rev. Fluid Mech.* 41, 181 (2009).
- [6]. Kawai, S. and Larsson, J., “Wall-modeling in large eddy simulation: length scales, grid resolution, and accuracy”, *Physics of Fluids*, Vol. 24, 2012.
- [7]. Liu, J.; Kailasanath, K.; Ramamurti, R.; Munday, D.; Gutmark, E.; Löhner, R., “Large-Eddy Simulations of a Supersonic Jet and Its Near-Field Acoustic Properties”, *AIAA Journal*, vol. 47, issue 8, pp. 1849-1864.
- [8]. Liu, J., Corrigan, A., Kailasanath, K., Pablo, M., Heeb, N., and Gutmark, E., “Computational Study of Shock-Associated Noise Characteristics Using LES”, *NRL Memorandum Report*, NRL/MR/6040-14-9560.
- [9]. Liu, J., Corrigan, A., Kailasanath, K.; Ramamurti, R.; Heeb, N., Munday, D., Gutmark, “Impact of Deck and Jet Blast Deflector on the Flow and Acoustic Properties of an Imperfectly Expanded Supersonic Jet”, *Naval Engineer Journal*, September, 2015, No. 127-3.
- [10]. Liu, J.; Corrigan, A.; Kailasanath, K.; and Gutmark; E., “Impact of Chevrons on Noise Source Characteristics In Imperfectly Expanded Jet Flows”, 21st AIAA/CEAS Aeroacoustics Conference, AIAA 2015-2835.
- [11]. Boris, J.P., and Book, D.L., “Flux-corrected Transport I: SHASTA a fluid transport algorithm that works”, *Journal of Computational Physics*, Volume 11. Issue 1. Pages: 38-69 (1973).
- [12]. Löhner, R., Morgan, K., Peraire, J., and Vahdati, M., “Finite element flux-corrected transport (FEM-FCT) for the Euler and Navier- Stokes equations,” *International Journal for Numerical Methods in Fluids*, Vol. 7, No. 10, 1987, pp. 1093–1109.
- [13]. White, F.M., “Viscous Fluid Flow”, McGraw-Hill Series In Mechanical Engineering, 1990.
- [14]. Spalding, D.B., and S.W., Chi, “The drag of a compressible turbulent boundary layer on a smooth flat plate with and without heat transfer”, *J. Fluid Mech.*, 1964, vol. 18, pp. 117-143.
- [15]. Aikens, K.M., Dhamankar, N.S., Martha, C.S., Yingchong S, Blaisdell, G.A., Lyrantzis, A.S., and Li, Z., “Equilibrium wall model for large eddy simulations of jets for Aeroacoustics”, AIAA-2014-0180
- [16]. Bras, S.L., Deniau, H., Bogey, C., and Daviller, G., “Development of compressible large-eddy simulations combining high-order schemes and wall modeling”, AIAA 2015-3135.
- [17]. Guillaume, A.B., Frank, E. H., Nichols, J.W. and Lele, S.K., “Nozzle Wall Modeling in Unstructured Large Eddy Simulations for Hot Supersonic Jet Predictions”, AIAA 2013-2142
- [18]. Hopkins, E. J. and Inouye, M., “An evaluation of theories for predicting turbulent skin friction and heat transfer on flat plates at supersonic and hypersonic mach numbers,” *AIAA J.* 9, 993–1003 (1971).
- [19]. De Graaff, D. B. and Eaton, J. K., “Reynolds-number scaling of the at-plate turbulent boundary layer,” *Journal of Fluid Mechanics*, Vol. 422, No. 1, 2000, pp. 319-346.
- [20]. Bridges J. and Wernet M.P., “The NASA Subsonic Jet Particle Image Velocimetry (PIV) Dataset”, NASA-2011-216807
- [21]. Geuzaine C. and Remacle, J. F., Gmsh: a three-dimensional finite element mesh generator with built-in pre- and post-processing facilities. *International Journal for Numerical Methods in Engineering* 79(11), pp. 1309-1331, 2009.

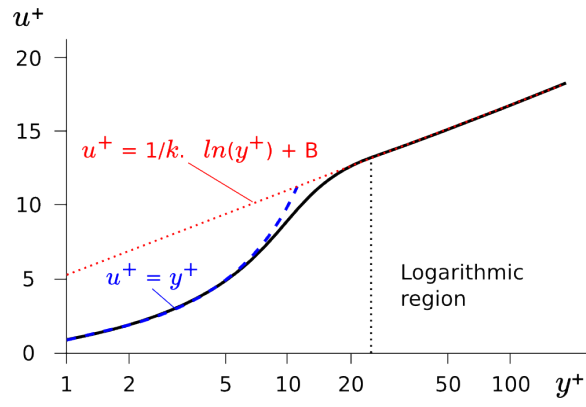


Figure 1. Velocity profile in an equilibrium turbulent boundary layer. The definition of  $u^+$ ,  $y^+$ ,  $k$  and  $B$  can be found in the section II.

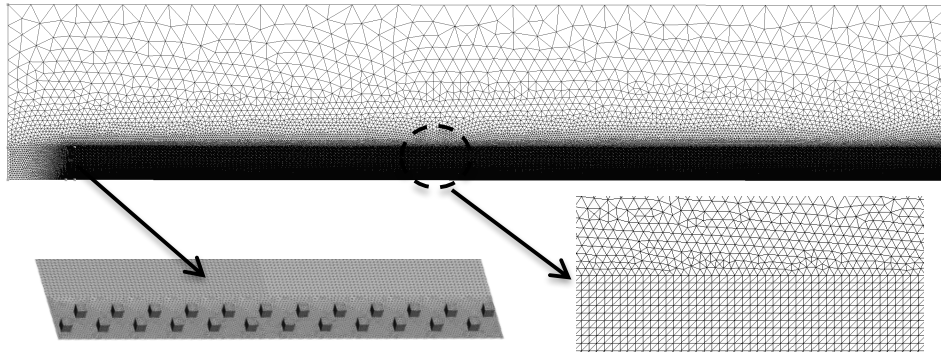


Figure 2. Mesh topology and wall surface roughness used in boundary-layer simulations on a flat plate.

Table 1. Mesh parameters at  $Re_\theta = 31000$  (using cubic cells)

	Mesh_I	Mesh_II	Mesh_III	Mesh_IV
$1^{st} \Delta y/\delta$	0.05	0.037	0.026	0.018
$1^{st} \Delta y^+$	465	370	245	150
Cells in BL	20	27	38	56

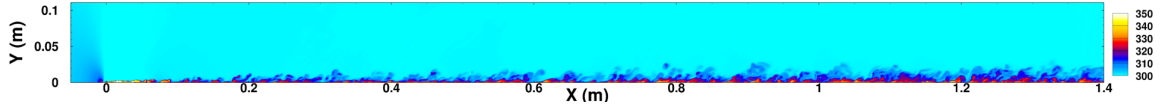


Figure 3. An instantaneous temperature distribution (using Mesh\_II in Table 1) of a boundary-layer flow at  $M_\infty = 0.9$  on a flat plate.

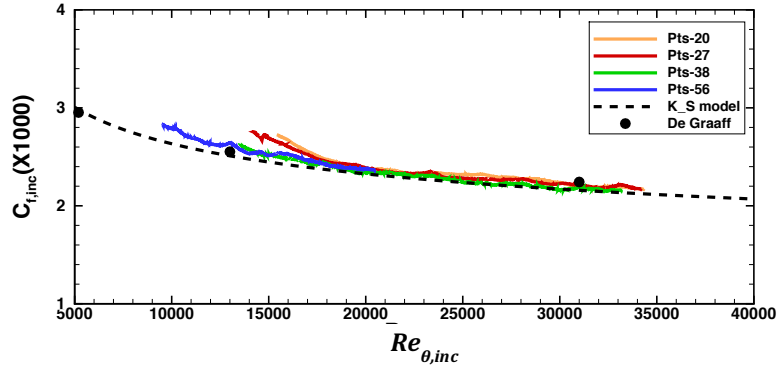


Figure 4. Axial evolution of the skin-friction in a boundary-layer flow at  $M_\infty = 0.9$  on a flat plate. The description of simulation data can be found in Table 1. The skin friction and the Reynolds number  $Re_{\theta,inc}$  are equivalent incompressible values estimated by the van Driest II transformation [13] shown in Eq. (4). Dashed line: *K'arm'an-Schoenherr* incompressible empirical correlation [18]. Symbols: incompressible experimental data from De Graaff and Eaton [19].

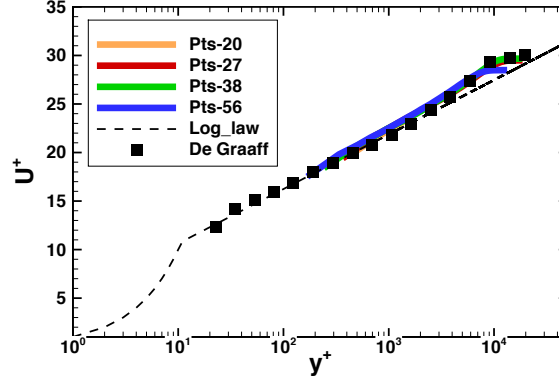


Figure 5. Streamwise velocity profiles. Predictions using the three coarser meshes are at the equivalent incompressible  $Re_{\theta,inc} = 31000$ . The result of the finest mesh is at  $Re_{\theta,inc} = 20000$ . The description of simulation data can be found in Table 1. Dashed line: logarithmic velocity profile shown in Eq. (2). Symbols: incompressible experimental data from De Graaff and Eaton at  $Re_{\theta} = 31000$  [19].

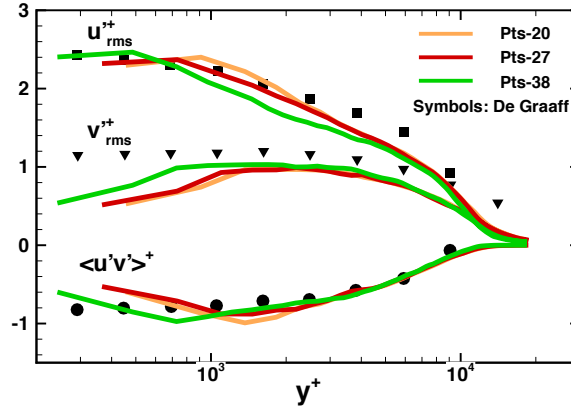


Figure 6. Comparison of turbulence intensities and the Reynolds shear stress at  $Re_{\theta,inc} = 31000$ . All quantities are in wall units. The description of simulation data can be found in Table 1. Symbols: incompressible experimental data from De Graaff and Eaton at  $Re_{\theta} = 31000$  [19].



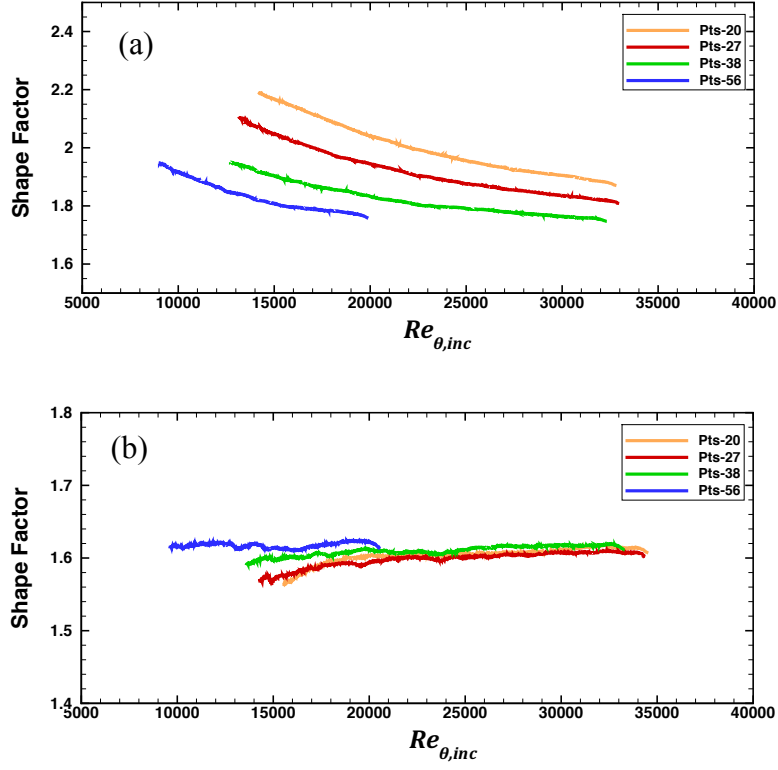


Figure 7. Axial distributions of the shape factor in a boundary-layer flow at  $M_\infty = 0.9$  on a flat plate. The description of simulation data can be found in Table 1. (a) In the first cell above the wall, the velocity and density are assumed to vary linearly with the vertical distance from the wall. (b) In the first cell above the wall, the velocity uses the equilibrium boundary-layer velocity profile shown in Figure 1 and the density profile follows the Crocco-Busemann relation.

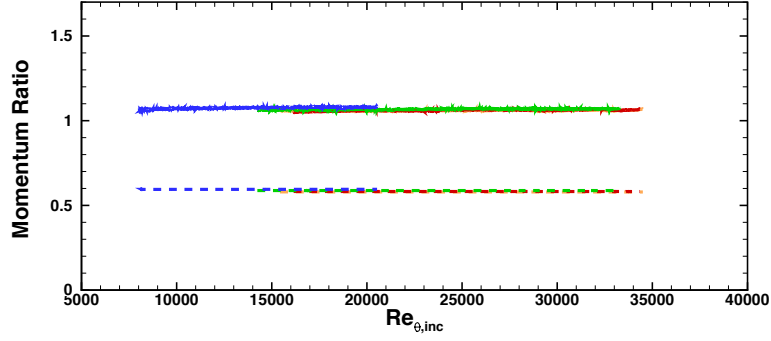


Figure 8. Ratios between the predicted momentum integrals ( $\int \rho u \, dy$ ) in the first cell above the wall and those derived from the equilibrium boundary-layer velocity profile (Figure 1) and the density profile based on the Crocco-Busemann relation. The solid lines: using a non-zero surface velocity. The dashed lines: using a zero-surface condition.

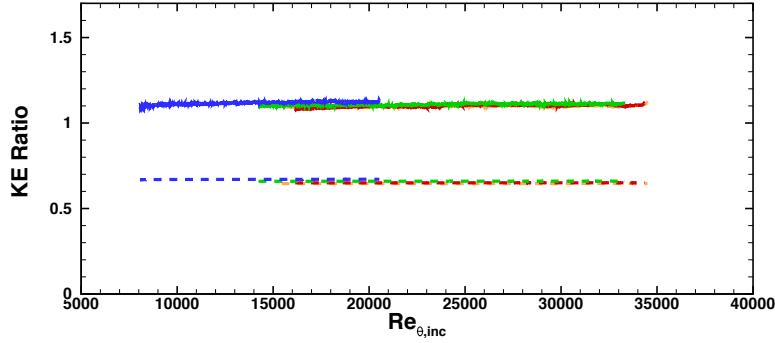


Figure 9. Ratios between the predicted kinetic energy integrals ( $\int \rho u^2 \, dy$ ) in the first cell above the wall and those derived from the equilibrium boundary-layer velocity profile (Figure 1) and the density profile based on the Crocco-Busemann relation. The solid lines: using a non-zero surface velocity. The dashed lines: using a no-slip condition.

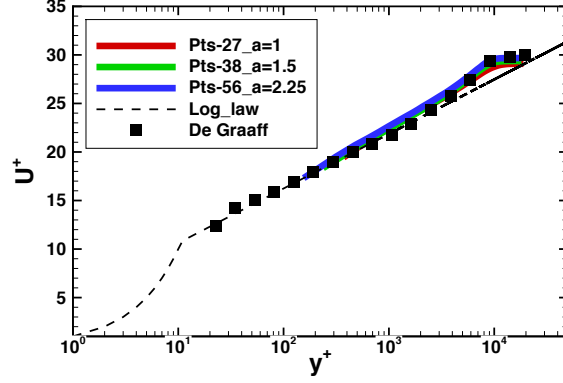


Figure 10. Comparison of streamwise velocity profiles at  $Re_{\theta,inc} = 31000$ . The cell size in the streamwise direction is fixed at  $\Delta x^+ = 370$ . The normal and the spanwise grid sizes ( $\Delta y = \Delta z$ ) vary, and there are three aspect ratios ( $\Delta x/\Delta y$ ). The description of simulation data can be found in Table 1. Dashed line: logarithmic velocity profile shown in Eq. (2). Symbols: incompressible experimental data from De Graaff and Eaton at  $Re_{\theta} = 31000$  [19].

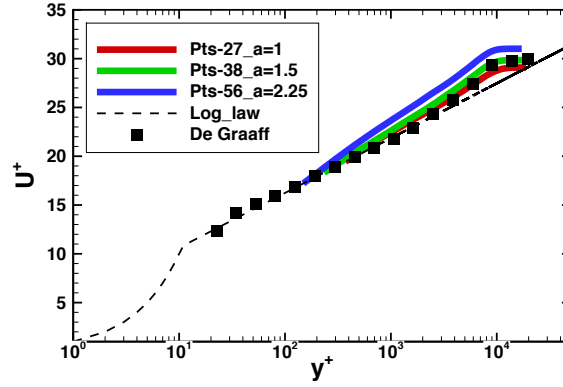


Figure 11. Comparison of streamwise velocity profiles at  $Re_{\theta,inc} = 31000$ . The cell sizes in both the streamwise and spanwise directions are fixed at  $\Delta x^+ = \Delta z^+ = 370$ . The normal cell size varies, and there are three aspect ratios ( $\Delta x/\Delta y$ ). The description of simulation data can be found in Table 1. Dashed line: logarithmic velocity profile shown in Eq. (2). Symbols: incompressible experimental data from De Graaff and Eaton at  $Re_{\theta} = 31000$  [19].



Figure 12. The converging and diverging nozzle geometry, the wall roughness shape and the boundary-layer mesh near the nozzle surfaces.

**Table 2.** Mesh parameters of the boundary-layer mesh slightly upstream of the nozzle lip.

	Mesh_I	Mesh_II	Mesh_III
$1^{\text{st}} \Delta y / \delta$	0.29	0.145	0.073
$1^{\text{st}} \Delta y^+$	280	140	70
Cells in BL	3~4	6~7	11~12

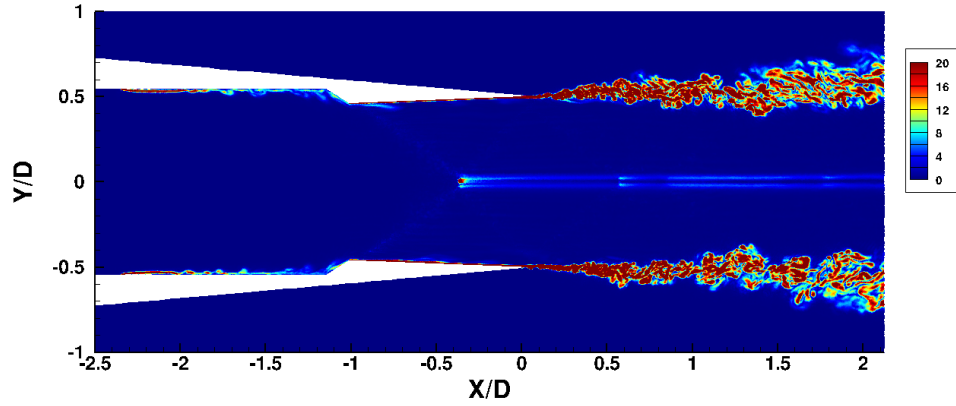


Figure 13. An instantaneous vorticity distribution  $\omega/(U_j \cdot D)$ .

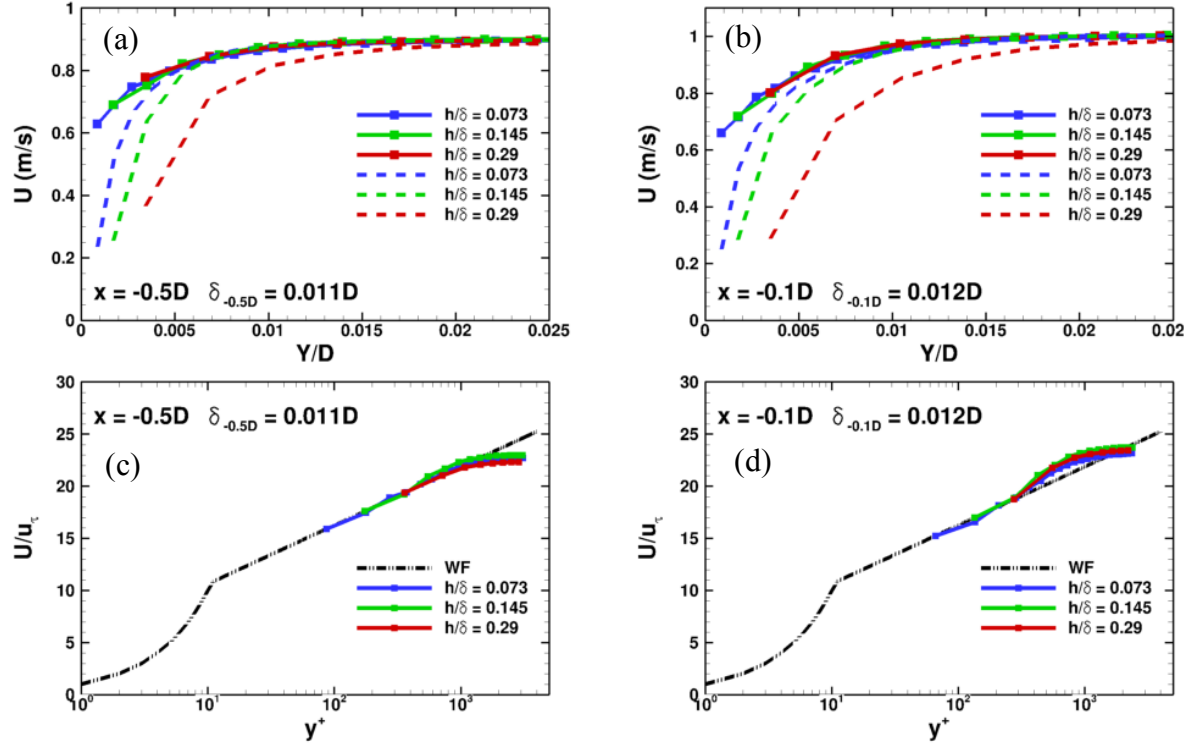


Figure 14. Axial velocity profiles at two axial locations upstream of the nozzle exit. “ $h$ ” is the vertical cell size  $\Delta y$  of the first cell adjacent to the wall.  $\delta$  is the boundary-layer thickness. (a)-(b) linear profiles. Solid lines are predictions using the wall-model method. Dashed lines are velocities of unresolved boundary layers, where the wall model is not implemented. (c)-(d) logarithmic profiles. The axial velocities are the van Deiest effective velocities [13]. The dash-dotted line is the logarithmic velocity profile defined in Eq. (2).

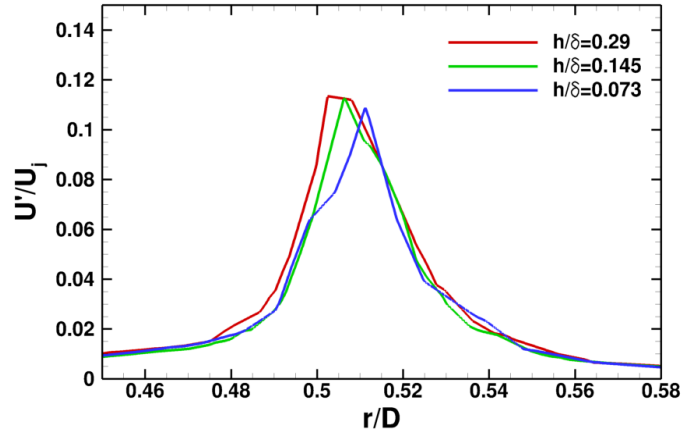


Figure 15. Radial turbulence intensity profiles slightly downstream of the nozzle exit at  $x = 0.1D$ . “ $h$ ” is the vertical cell size  $\Delta y$  of the first cell adjacent to the wall.  $\delta$  is the boundary-layer thickness.